
A PHYSICS-GUIDED NEURAL NETWORK FOR FLOODING AREA DETECTION USING SAR IMAGERY AND LOCAL RIVER GAUGE OBSERVATIONS

A PREPRINT

Monika Gierszewska, Tomasz Berezowski*

October 14, 2024

ABSTRACT

The flooding extent area in a river valley is related to river gauge observations. The higher the water elevation, the larger the flooding area. Due to synthetic aperture radar's (SAR) capabilities to penetrate through clouds, radar images have been commonly used to estimate flooding extent area with various methods, from simple thresholding to deep learning models. In this study, we propose a physics-guided neural network for flooding area detection. Our approach takes as input data the Sentinel 1 time-series images and the water elevations in the river assigned to each image. We apply the Pearson correlation coefficient between the predicted sum of water extent areas and the local water level observations of river water elevations as the loss function. The effectiveness of our method is evaluated in five different study areas by comparing the predicted water maps with reference water maps obtained from digital terrain models and optical satellite images. The highest Intersection over Union (IoU) score achieved by our models was 0.89 for the water class and 0.96 for the non-water class. Additionally, we compared the results with other unsupervised methods. The proposed neural network provided a higher IoU than the other methods, especially for SAR images registered during low water elevation in the river.

1 Introduction

Flooding is one of the most common natural phenomena occurring and impacting people's lives and the environment around the whole world. One important aspect of flood monitoring is estimating its extent to calculate economic losses and investigate the effect on the natural environment. Currently, the flood monitoring methods include hydrological station monitoring, hydrodynamic modeling, and remote sensing monitoring. The first method is characterized by high accuracy; however, it is limited by the number of gauge stations, and it monitors the situation only in a small area. Hydrodynamic modeling is the most accurate method of estimating flooding extent, however, it requires excessive study site parametrization along with the monitoring data. The remote sensing methods are currently often applied due to their increasing temporal resolution and ability to monitor floods in large areas with sparse monitoring networks [1, 2]. Remote sensing data from both passive and active sensor types were successfully applied in flood mapping, however, due to the frequent cloud cover and rain during flood events, the number of available cloudless optical images is strongly limited. These limitations do not hold for the Synthetic Aperture Radar (SAR) data. Therefore, SAR data is currently gaining more and more popularity in flood mapping applications.

1.1 Background and related work

Contemporary methods of flood mapping using SAR images can be grouped based on the mapping technique. An effective tool for delineating the inundated areas is thresholding of SAR backscattering [3]. The threshold can be determined in an automated way [4] or by expert judgment [5]. The computational efficiency of this method makes

*The authors were with the faculty of Electronics, Telecommunications and Informatics, Gdańsk University of Technology, Gabriela Narutowicza 11/12, 80-233 Gdańsk, Poland, e-mail: tomberez@eti.pg.edu.pl

it suitable for rapid mapping purposes; however, its performance decreases in the case of large-area water bodies [6], complex topography, or dense vegetation occurring in the study area.

In contrast to pixel-based thresholding, image segmentation techniques were proposed. They offer the advantage of using the spectral-spatial-related characteristics of the parameters of the segments. Horrit et. al. [7] used the statistical active contour method to delineate a flood. However, this algorithm requires manual initialization of the contour close to the edge of the object being segmented. Martinis et. al. [8] proposed the split-based approach what is an automated method and offers some advantage over the thresholding.

Another common technique is image change detection, usually performed by comparing pre- or post-disaster reference data with flood imagery [4, 9] by image difference, normalized difference, image ratio, and log-ratio [10, 11]. Shen et al. [12] proposed an improved change detection (ICD) method that uses multiple (~5) pre-flood SAR images and a multi-criteria approach, which leads to minimization of false positives caused by water-like bodies and reduces the effect of speckles.

In general, the flood mapping approaches are based on a single or dual image (pre- and post-event). Time-series data are less commonly applied; however, utilizing this has been very useful in studies focusing on flood monitoring and ecology [13–15] and hydrodynamic model calibration and validation [16]. Multi-temporal images also help reduce seasonal noise in the reference image [17]. The pixel-wise methods using time-series data are dependent on calculated features or manual threshold adjustment and do not consider neighboring pixels [18]. Compared to them, deep learning methods can easily learn patterns in spatial and temporal contexts without the process of feature selection, based only on SAR polarization images.

Recently, most of the proposed flood mapping methods have been based on applying deep learning models performing semantic segmentation, which solved image segmentation at the semantic level and classified images at the pixel level. The growth of its usage is caused by the introduction of a convolutional neural network (CNN) that has shown promising results in SAR data classification [19, 20]. In the literature, there are many studies regarding flood or water mapping methods that apply different deep learning architectures. For example, Rizwan et al. [21] investigated the performance of U-Net and FCN. As shown in their study, deep learning models performed better than Otsu due to the generalization capabilities of deep learning-based segmentation models. Another study investigated the accuracy of FWENet model water body extraction compared to the UNet, Deeplab v3, and UNet++ models [22]. FWENet performed the best due to applied dilated convolution. Another approach proposed a multimodal OmbriaNet architecture, which employed satellite data from various sensor types and timestamps (pre- and post-event images) [23].

1.2 Aim and motivation

Several studies showed the benefit of connecting the data from hydrological and satellite monitoring. The river gauge observations, such as water elevation and discharge, are related to the flooding extent area in a river valley [24]. The higher the observed water elevation or discharge, the larger the flooding area. For example, researchers used the flooding extent maps to derive time series of river discharge estimates in several British Columbia (Canada) [25] and South Korea [14] rivers. Another study related the river gauge observation in the Congo River (Africa) with SAR backscatter using satellite altimeter data instead of measured water elevations [26]. Yet another study demonstrated that the relation between inundation extent and river gauge observations can be conversely used [27, 28]. The results showed that the relation is close to linear, and hydrological observation can be applied to SAR-derived flooding extent mapping.

The presented supervised deep learning approaches provide highly accurate results. However, they require data annotation, for which acquisition is a time-consuming process that demands expert knowledge. To overcome this limitation, some unsupervised deep learning methods were proposed. One example of an unsupervised method is a model based on a spatiotemporal variational autoencoder that was trained with reconstruction and contrastive learning techniques [29]. Apart from their successes in flood detection using SAR imagery, this approach is weakly supervised and still relies on training/labeled samples. Another approach combined super-pixel and CNN to map floods using SAR imagery and routinely available ancillary datasets [30]. This method was applied only for VV-polarized SAR data that have an influence on the discrimination between flooded and non-flooded areas. Similarly, for single-polarized SAR data, another study presented a fully automated approach, including the process of obtaining training labels from auxiliary data such as DTM and optical images, and the supervised deep learning model [31]. Despite the described approaches, there is still a need to develop unsupervised machine-learning techniques for water extent mapping on time-series satellite data [20, 32].

Most of the presented studies performed the detection task of water extent during flood events. The supervised deep learning methods were usually trained with satellite images showing flood areas. However, the studies did not show the efficiency of water area mapping of the proposed methods for images acquired during non-flood conditions. Some

other research showed the algorithms for river channel detection [33–35]. These methods extracted rivers of SAR images registered for low water elevation accurately. However, there are no experimental results of mapping accuracy in the case of inundated areas occurring in the river valley. Hence, it will be valuable to perform a method that will be efficient in water area detection regardless of the water elevation in the river.

One of the new trends is to integrate domain knowledge and achieve physical consistency by teaching machine learning models about the governing physical rules of the Earth system. This approach, known as physics-guided neural networks (PGNN), combines deep learning with physics-based models. PGNNs can be created in two different ways: by combining the training data with the results of the physical model or by adding to the cost function the physical formula that ensures that the predictions are physically consistent. An example of a PGNN approach is a time-varying lake temperatures model [36]. In particular, that study integrated the physical relationships between the temperature, density, and depth of water into the PGNN. Another example of a PGNN integrated augmented satellite image samples with pixel-level physical parameters derived from Landsat 8 images for water leak detection in canals [37]. Yet another study built a CNN model architecture inspired by polarimetric features for SAR image classification [38]. The PGNN approach outperformed the deep learning models regarding prediction accuracy, especially with a limited input dataset [39].

Our study aimed to create an unsupervised method for water extent mapping that would help to identify river and non-river flooding in locations with sparse observation networks, various climate conditions, and different land-cover types. We use the Sentinel 1 time series SAR images in VV and VH polarization as input data and water elevation data from river gauges as labels. Based on the described studies [14, 24–27], we can assume that there is a monotonically non-decreasing relation between a local river water elevation and the flooded area, and it is close to linear. This dependence can be quantified using the Pearson correlation coefficient. We utilize the dataset to train the physics-guided neural network for flooding area detection (FPGNN). By applying the correlation coefficient between local water elevation and water area on SAR images as a loss function in the neural network, we show that the model predictions are consistent with the assumption. Next, we quantify the model performance with ground truth data from DTM and optical images. In the final step, we compare our method to other automated approaches and discuss the results depending on the study areas' characteristics.

2 Study areas and datasets

This section outlines the study areas, the acquisition of the input data (hydrological and SAR data), the preprocessing steps applied to the SAR data, and the reference data used in the validation process.

2.1 Study sites

To show the performance of our method, we chose five study cases that varied by climate, river width, and land use. The first case shows the Parana Madeirinha River located in Brazil, in the period January 2019 to December 2022 (119 images). The climate is tropical monsoon, and the land use is forest, barren, and urban. The width of the riverbed is approximately 280 m, and the maximum difference in water level is 12.59 m. The chosen water station is located in Autazes city (59.1° W, 3.6°S). The second case is the Mekong River located in Cambodia, in the period March 2017 to December 2018 (130 images). The climate is tropical savanna, and the land use is mostly agricultural land with small villages along the river. The width of the riverbed is approximately 500 m and the maximum difference in water level is 8 m. The hydrological observation was obtained from a gauge located in Prek Kdam city (104.8°E, 11.8°N). The third case contains four floods that occurred on the Po River in Italy, in the period November 2014 to October 2020 (120 images). The climate is humid subtropical, and the land is covered by agricultural fields and forests. The river is about 200 m wide. The water gauge station is located under the bridge near Valenza city (8.6°E, 45°N) and the maximum difference in water level is 5.70 m. The final two study cases are located in England (Derwent River – 144 images) and Poland (Warta River – 145 images) with oceanic and humid continental climates, respectively. Floods on both rivers occur usually during the winter and spring seasons. Most of the areas are agricultural and there are flood embankments along both rivers. The main difference between these study cases is in the width of the rivers – 20 m in England and 100 m in Poland. The water elevation data used were measured at the Bubwith (-0.9°W, 53.8°N) and Świerkocin (15°E, 52.6°N) stations, respectively.

2.2 SAR Data and Processing

The Sentinel-1 radar mission is composed of a constellation of two satellites, Sentinel-1A (launched on 3 April 2014) and Sentinel-1B (launched on 25 April 2016). The revisit time depends on the region; the longest is at the equator, at 6 days. Sentinel-1 sensors transmit C-band waves in dual-polarization mode and the data are freely available.

In this study, we used the Level-1 Ground-Range Detected High-Res Dual-Pol (GRD-HD) Sentinel 1 products in the interferometric wide swath (IW). We searched for the Sentinel 1 data available for different time ranges for each test site on the Alaska Satellite Facility (ASF). We used Radiometrically Terrain Corrected (RTC) Sentinel-1 products preprocessed on-demand by the ASF Hybrid Pluggable Processing Pipeline (HyP3) [40]. Processing with this software consisted of five steps: co-registration to the DEM file, radiometric calibration to the backscatter coefficient (γ_0) [dB], speckle filtering using the Enhanced Lee filter in a 7×7 pixel kernel, range-Doppler terrain correction with projection to the UTM coordinate system with proper zone, and finally cropping the images to the proper bounding box of the study area. Every downloaded image contained two bands: Gamma0_VV and Gamma0_VH. The spatial resolution of the images was 10 m and the image size was different for each study area.

2.3 Hydrological Data

We obtained daily hydrological data from the gauge station located in each of the study areas [41–45]. The water elevations were directly measured on the gauge. We recalculated the water elevations in the validation step by adding a height above sea level zero of the water gauge to the measured elevations.

2.4 Reference Data

1) Elevation Data

We used the 30 m Copernicus DEM for the Cambodia and Italy sites. For the relevant area of Brazil, the Copernicus DEM had inaccurate elevation due to registration during high water elevation in the river. Therefore, we chose elevation data provided by the Shuttle Radar Topography Mission (SRTM) for this site. For areas in Poland and England, the digital elevation models produced by government agencies [46, 47] were used, because they had higher spatial resolution than the Copernicus and SRTM DEMs.

2) Optical Data

As the source of optical data, we chose the Landsat 8 (L8) Operational Land Imager (OLI) and the Sentinel-2 (S2) MultiSpectral Instrument (MSI). The images were acquired by Sentinel Hub API. We filtered the images by collection (Sentinel 2 L2A, Landsat 8 L2A), acquisition time (the same time range as for the Sentinel 1 data), percentage of cloud cover, and area of interest. Next, we calculated the Modified Normalized Difference Water Index (MNDWI) [48] using bands 3 and 6 for the L8 data and bands 3 and 11 for the S2 data. Then, we resampled the optical data to 10 m resolution and clipped them to the same area as the SAR data. Additionally, we manually selected the clouds and cloud shadows pixels on the optical images.

3 Methodology

In this section, we introduce our proposed approach to water extent mapping by describing the architecture of the proposed neural network and validation steps. The PGNN model architecture is outlined in Fig. 1.

3.1 Network architecture

Our method for mapping the extent of the water is based on the FCN-8 fully convolutional network [49] architecture, which was one of the first CNN architectures for semantic segmentation. We built our algorithm by reducing the number of layers in the FCN architecture and adding regression layers. In our FPGNN architecture, we can highlight three modules. The first module, named the feature-extraction module, produces the features obtained from input data by convolutional function and image size reduction. This part of the network consists of six 3×3 convolutional layers with the ReLU activation function and three 2×2 average pooling layers with stride 2.

Next, as in a FCN, the output of the first module is used as input to the deconvolutional layers, which restore the small size feature maps to their original size. We also inserted an “add” layer that sums the deconvolved output and the convolved output (from the feature extraction module in which number of channels is earlier averaged to one channel using a 1×1 convolutional layer). The upsampling part contained three 4×4 deconvolutional layers with ReLU activation and stride 2, three “add” layers and one 1×1 convolutional layer to integrate the output of the previous layer into a consistent features set. The output of the convolution layers was padded with zeros to ensure that the size of the last two-dimensional layer in our network is the same as the input size. The purpose of the last convolutional layer was to provide the water body segmentation map, **hereinafter named the water mask**. Therefore, in contrast to the

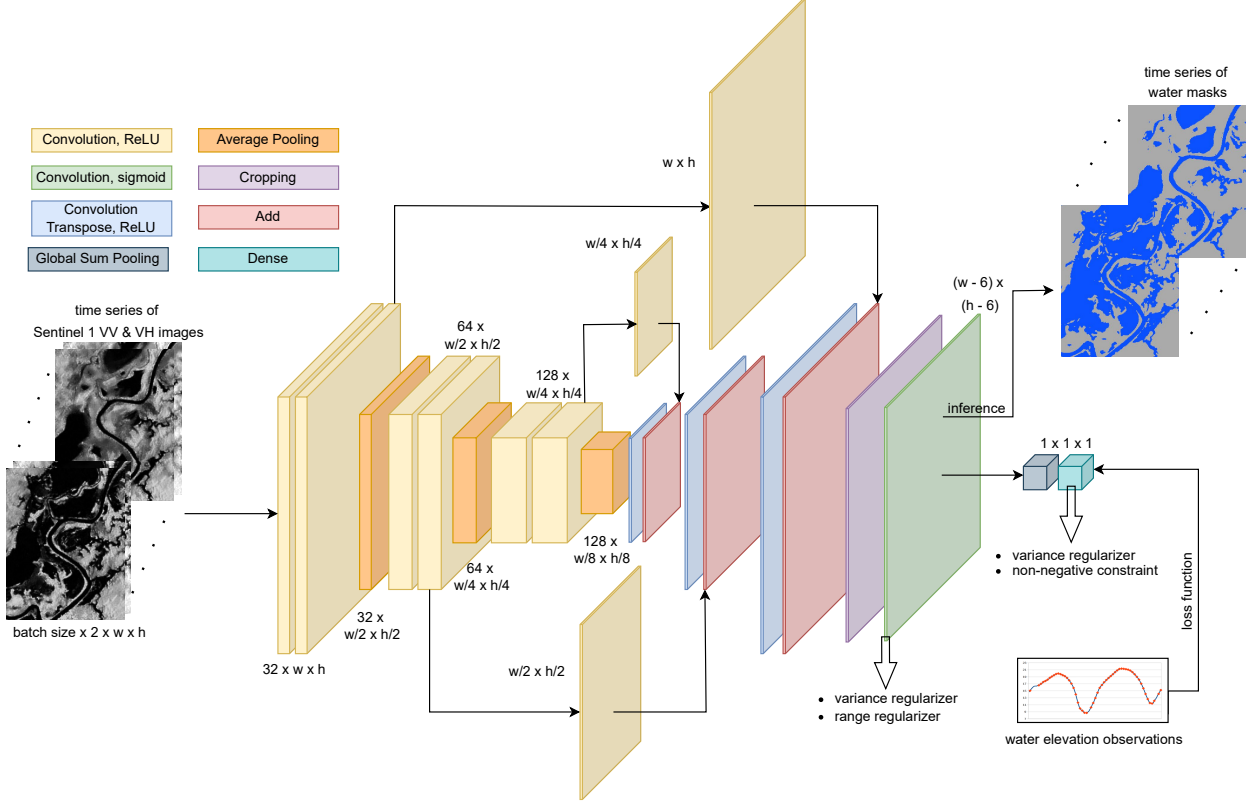


Figure 1: Architecture of the FPGNN model.

softmax function that was applied in the FCN, the activation function used here was sigmoid, which is commonly used in binary segmentation task because the output of this function will range between 0 and 1.

The last part of the architecture is the regression module. It includes a global sum pooling layer that sums all pixels from the water mask to one value. The calculated sum is the input to the last fully connected layer without an activation function to get the final output (water extent area), which is evaluated against the ground truth local water elevation by a correlation loss function (eq. 1).

3.2 Training Algorithm

Our dataset for each test site contained time-series of dual-pol (VV+VH) radar images with sizes depending on the study sites, and the corresponding time-series of local water elevations. This dataset was divided into training and testing sets with an 80% to 20% ratio. The radar data presented the riverbeds at different stages: low, average, or high. Hence, we used stratified sampling to ensure that samples for various water elevations were present in both the training and test sets.

In model training, we used the Adam optimization algorithm with a learning rate of 0.01. The batch size used was equal to half the number of samples available in the training set. As a loss function, we adopted (eq. 1) the Pearson correlation coefficient (PCC) between the predicted sum of the water mask area, i.e., the output of the global sum pooling layer (\hat{y}), and the local water level observations (y) of river water elevations.

$$Loss = 1 - \frac{\sum_{i=1}^n (\hat{y}_i - \bar{\hat{y}})(y_i - \bar{y})}{\sqrt{\sum_{i=1}^n (\hat{y}_i - \bar{\hat{y}})^2} \sqrt{\sum_{i=1}^n (y_i - \bar{y})^2}} \quad (1)$$

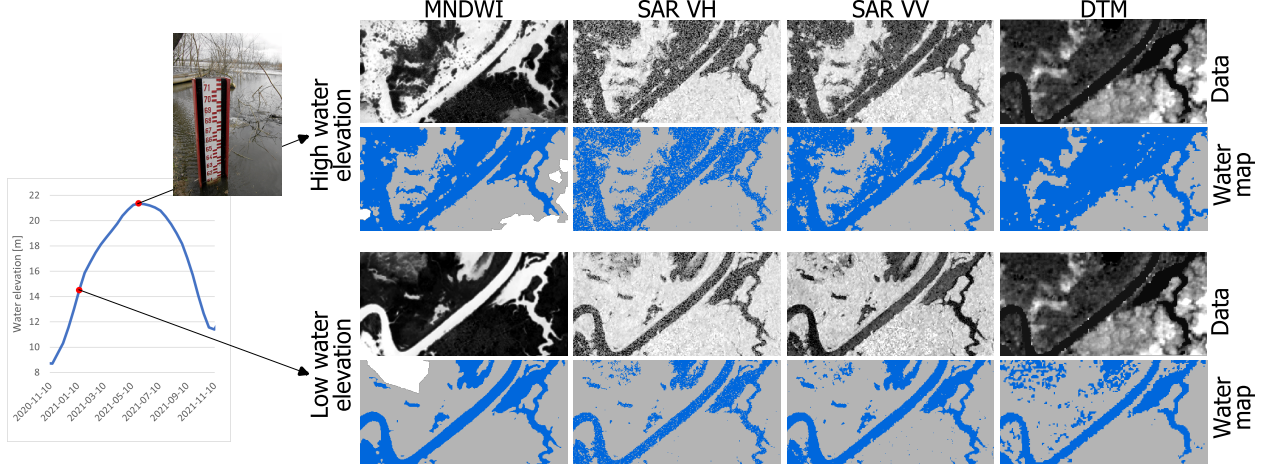


Figure 2: Visual comparison of water masks obtained by thresholding from various spatial data and the effect of water elevation in the river on the water extent area.

where n is the set size, $\bar{\hat{y}}$ is the mean value of \hat{y} , and \bar{y} is the mean value of y . The values of PCC are always between -1 (negative correlation) and 1 (positive correlation). A value of 0 indicates that there is no correlation between the two variables.

As the model is trained without labeled data, we added a modification to the network training to help it make predictions. In the last model layer, i.e., the global sum pooling, we added a kernel constraint that maintains the nonnegative weights. This ensures that the model set higher values for each water pixel than for each non-water pixel in the output of the upsampling module. Effectively, the water pixels in the water body segmentation map are forced to converge to one and non-water pixels converge to zero. Our model sometimes tended to provide the wrong prediction despite the obtained high correlation coefficient of the training and validation sets. For example, the difference in values of water and non-water pixels in the output result of the upsampling module were very low, or the model did not retrieve all pixel values after the deconvolution layers in the output of the upsampling module. To avoid these, we created a custom activity regularizer that applies a penalty to the layer’s output. The penalty is calculated for the batch and divided by the batch size. In the fully connected layer, we applied the activity regularizer calculated by $\frac{1}{0.01 * \sigma^2}$, where σ^2 is the variance of the predicted output. Another custom activity regularizer (eq. 2) was added to the convolutional layer with the sigmoid activation function, i.e., the water mask, as:

$$reg = 10 * \frac{1}{\max(x) - \min(x)} + 100 * \sigma_{clip}^2 \quad (2)$$

where x is the layer output and σ_{clip}^2 is the variance calculated for the subset of the layer output (the matrix of 6x6 pixel size belonging to the non-water class on each dataset sample). We applied the early stopping method in the training process. This method stops training when a monitored metric (validation loss) has stopped improving. We also added a new condition that checks the difference in the maximum and minimum values in the output of the upsampling module. The training is stopped if the difference is higher than 0.9 and the validation loss does not improve. If the difference is lower, the training is continued. This condition improves the result of the output of the upsampling module that produces the water body segmentation map. We trained the network for each study area separately, producing five trained models. Based on each trained model, we created an intermediate model for inference with the last convolutional layer with a sigmoid function as the output layer. Due to that, the inference outputs were images with sizes the same as the input radar images representing a soft classification of water extent with pixel values between 0 and 1. Hard classification of water extent was obtained using thresholding. We tested the effects of various thresholds in range from 0.1 to 0.55, where the pixels with a value above or equal to the threshold were labeled as water class and pixels with values below the threshold were classified as non-water class.

3.3 Validation Process

1) Validation using DTM-based water mask

The water mask for the DTMs was extracted by labeling as water the pixels with values lower than the water elevations recalculated to zero-gauge level (Fig. 2). The time-series-masked DTMs were provided for the same days as the SAR

images, except for days when the measured water elevation was lower than the elevation in the river pixels present in a DTM. Effectively, a binary water map for the same extent as the SAR images was produced. However, this method was only valid for rivers with a gentle bed slope. In these cases, the difference between the extrapolated water extent assuming no riverbed slope and the true water extent was smaller than one SAR pixel. For the rivers with steep riverbed slopes, which in our case are located in Poland, England and Italy, we limited the DTM-based validation to the extent near the water gauge.

2) Validation using MNDWI water mask

To produce the water mask for the optical data, we used the MNDWI images. In the MNDWI data, pixels with a value larger than zero are classified as water (Fig. 2). However, the appropriate threshold depends on the sensor, imaged region, and acquisition time [50]. Hence, we calculated the threshold for each MNDWI image using the Otsu thresholding method. The Otsu method automatically determines the global threshold to separate pixels into two classes by minimizing the variance between classes [51]. In the cases where the image histogram was not bimodal, we performed manual thresholding. Subsequently, we applied the clouds mask and cloud shadows mask to the resulting maps.

3) Validation metric

The ground truth and predicted water cover maps were compared using the Jaccard index, also named Intersection over Union (IoU, eq. 3). It measures the similarity between two binary images.

$$IoU_n = \frac{A_{P,R}}{A_P + A_R - A_{P,R}} \quad (3)$$

where A_P is the area of n class on the predicted mask, A_R is the area of the n class on the reference mask, and $A_{P,R}$ is the area of intersection of the n class on both masks. In our case, the n class was either water or non-water. The values of IoU range from 0 to 1, where zero means that the masks do not intersect, and one means that the masks completely overlap.

4) Benchmarking methods

To investigate the effectiveness of our algorithm, we compared it with other fully automatic methods, such as Otsu thresholding, Chan-Vese algorithm, gaussian mixture model (GMM), and spectral clustering (SC). In each of these methods, we applied SAR images converted to dB. In the Otsu method, we calculated the Otsu threshold and used it to create the water masks. The Chan-Vese segmentation algorithm is a technique for image segmentation based on the level set method, particularly effective for segmenting objects with blurry or poorly defined boundaries. It is a region-based segmentation model that works by minimizing an energy functional to detect the boundaries of objects within an image [52]. The next method we applied was the Gaussian mixture model. It is an unsupervised clustering algorithm that assumes input data conforms to a normal distribution. The GMM models the mixture distribution of input data as follows [53] :

$$p(x) = \sum_{c=1}^M \pi_c \cdot 1.N(x|\varepsilon_c, \Sigma_c) (0 \leq \pi_c \leq 1) \quad (4)$$

where x refers to D-dimensional observation data; M is the total number of mixture components; π_c is the weight factor of c -th mixture component and satisfies $\sum_{c=1}^M \pi_c = 1$. $1.N(x|\varepsilon_c, \Sigma_c)$ represents the estimated Gaussian density of c -th mixture component, and the parameters ε_c and Σ_c are its mean vector and covariance matrix, respectively. The last method was spectral clustering. Unlike traditional clustering algorithms like K-means, which rely on distance-based criteria, spectral clustering works by utilizing the eigenvalues and eigenvectors of a similarity graph to cluster the points. It is very useful when the structure of the individual clusters is highly non-convex [54].

4 Results and Discussion

This section includes the analysis of results and water extent maps obtained with our methodology. It also contains an evaluation of the efficiency of our approach compared to other methods.

4.1 Results of validation process

The threshold used to create the binary masks from the FPGNN results ranged between 0.1 and 0.55 with a 0.05 step. Pixels with values below the threshold were classified as non-water, and pixels above or equal to the threshold

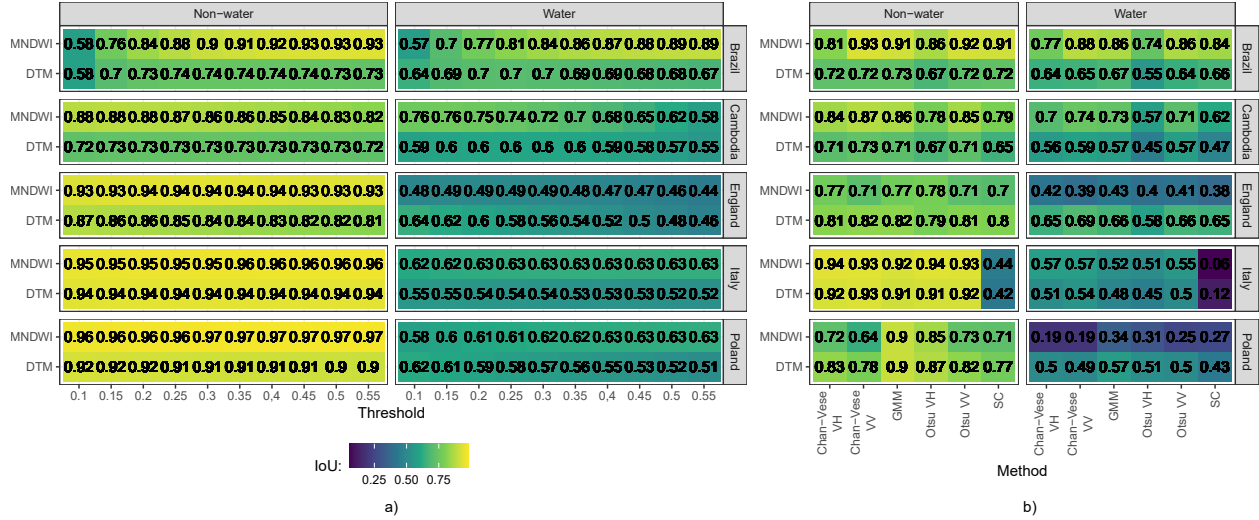


Figure 3: Average IoU values of water and non-water masks produced by FPGNN models (a) or benchmarking methods (b). Panels are varied by the study sites (columns) and class (rows). Within each panel, the IoU value is shown per threshold used in hard classification or benchmarking method (panel columns) and reference water mask (panel rows).

were labeled as water class. The IoU values were obtained for each SAR image with accompanying DTM-based or MNDWI water mask and averaged in the study period. Depending on the threshold applied in the validation process, the IoU values obtained were different (Fig. 3a). For areas located in Poland and England, the average IoU of the water class in validation with the DTM decreased as the threshold increased. In contrast, in Brazil’s example, the IoU was the highest for the 0.35 threshold. The IoU values did not change significantly depended on the threshold for the Cambodia and Italy areas. In the case of the MNDWI validation, the IoU for the water class was greater for a smaller threshold in the Cambodia and England areas. The threshold did not have a significant impact on the results for the Italy region, where the IoU values differ by only about 0.01 regarding on threshold. The increasing threshold increased the IoU values considerably in the Brazil model and slightly in the Poland model. In terms of the ground truth data used in the validation, the average IoU for both classes were usually higher for comparison results with the MNDWI images than with the DTM (except for the water class in the England study area). Significant differences ($p < 2.2 * 10^{-16}$) between the IoU for the MNDWI and DTM occurred in the Brazil and Cambodia study areas, where the elevation data applied had a spatial resolution of 30 m.

The main advantages of DTM water masks are their availability with the same frequency as hydrological observation and the detection of water beneath vegetation. However, the accuracy of the obtained water extent depends strongly on the spatial resolution, the occurrences of areas located below the water elevation outside the river valley, and the slope of the riverbed. Another disadvantage is that this method does not take into account water areas resulting from other sources than high-water elevation in the river, such as heavy rainfall. Therefore, water masks from the DTM are accurate only for the area near the water gauge station and using high-quality elevation data. With the method of thresholding the MNDWI images, one of the most important limitations is the time resolution. The availability of optical images is strongly limited by clouds, which often occur during flood events. Additionally, the acquisition day of optical and radar images should be the same due to the fact that flooding is a dynamic phenomenon (in our study, we accepted a max +/- 4 days difference if no radar image was acquired during the flood). Also, monitoring the presence of water under vegetation is limited with optical satellite images, like similar with SAR images registered in the C band, which is characterized by reduced canopy-penetrating ability [55]. In our study, the water masks from the MNDWI data overlap more with the water masks from the SAR images than from the DTMs, which confirmed the results from the validation process (Fig. 3a).

The overall average IoU of FPGNN for MNDWI validation ranged between 0.57 (Brazil model with a threshold of 0.1) and 0.91 (Brazil model with a threshold of 0.5 and 0.55). For the average IoU calculated per class, the water class had the highest average IoU (0.89) for the Brazil model with a threshold of 0.5 and 0.55 in validation with the MNDWI (Fig. 3a). The lowest average IoU for the water class (0.44) was for the England area, with a threshold of 0.55. The non-water class was classified more accurately than the water class. The highest IoU for this class was 0.95–0.97 for comparison of the model’s Poland and Italy results (threshold 0.1–0.55) with the MNDWI, and the lowest was 0.58 in MNDWI validation of the Brazil model outputs thresholded at a value of 0.1.

The highest IoU (0.89) of the Otsu method (Fig. 3b) obtained in MNDWI validation was for the VV data of the region in Brazil. However, the lowest IoU (0.49) was obtained for the VV images from Poland in comparison with the MNDWI water masks. Regarding the IoU per class, the highest IoU of the water class was for the Brazil model performed with VV data (0.86) and the lowest was for the Poland area, also with VV images (0.25). The non-water class provided the highest IoU for the VH Italy data (0.94), and the lowest for the England VV data (0.71).

In case of Chan-Vese segmentation, the highest IoU (0.90) for MNDWI validation was for the VV data of the region in Brazil. However, the lowest IoU (0.42) was obtained for VV images from Poland in comparison to the MNDWI water masks. In case of IoU per class, the highest IoU of the water class was in the Brazilian model performed with VV data (0.88) and the lowest for the Poland area also with VH and VV images (0.19). The non-water class provided the highest IoU of the VH Italy data (0.94) and the lowest for the Poland VV data (0.64).

The Gaussian mixture model provided the highest IoU (0.88) for MNDWI validation for the region in Brazil. However, the lowest IoU (0.6) compared to the MNDWI water masks was obtained for the Poland area. In the case of IoU per class, the highest IoU of the water class was in the Brazil model (0.86) and the lowest for the area of Poland (0.34). The non-water class provided the highest IoU for Italy data (0.92) and the lowest for England (0.77).

In the case of the spectral clustering method, the highest IoU (0.88) for MNDWI validation was the region in Brazil. However, the lowest IoU (0.25) in comparison with MNDWI water masks was obtained for the area of Italy. In the case of IoU per class, the highest IoU of the water class was in the Brazil model (0.84) and the lowest for the Italy area (0.06). The non-water class provided the highest IoU for Brazil data (0.91) and the lowest for Italy (0.44).

From benchmarking methods, the highest IoU values for MNDWI validation were obtained from the Chan-Vese method applied to VV data (Brazil, Cambodia, and Italy study areas) and the Gaussian mixture model (England and Poland study areas). The evaluation of the water masks with MNDWI images showed that the FPGNN outputs, which obtained the highest average IoU from tested thresholds (0.5 for Brazil, 0.2 for Cambodia, 0.15 for England, 0.3 for Italy, 0.2 for Poland), provided equal IoU values to best benchmarking methods for the Brazil and Cambodia data. The higher IoU than other unsupervised methods, the FPGNN obtained for Italy (0.04), England (0.11) and Poland (0.16) areas.

For the DTM validation, the lowest average IoU obtained by FPGNN was 0.61 for Brazil, with a threshold of 0.1 and the highest was 0.77 for Poland, with a threshold of 0.1. The average IoU values calculated per class were higher for the non-water class, except for the Brazil site. The water class had the highest average IoU (0.7) for the Brazil model, with a threshold of 0.2–0.35 (Fig. 3a). The lowest average IoU (0.46) was in comparison with the DTM for the England area with a threshold of 0.55. For the non-water class, the highest IoU was 0.94 for the Italy results (threshold 0.1–0.55), and the lowest was 0.58 for the Brazil model outputs thresholded at a value of 0.1.

With the Otsu algorithm, the highest average IoU was 0.73 for the England model trained with VV images, and the lowest (0.56) was obtained for the VH Cambodia dataset. The water class had the highest IoU (0.66) for the England VV images and the lowest (0.45) for the VV data from Cambodia and Italy. The IoU for the non-water class in DTM validation ranged between 0.67 (the results of the VH bands for Cambodia and Brazil) and 0.92 (the results of the VH bands for Italy) (Fig.3b).

In the case of the Chan-Vese method, the highest IoU (0.75) provided for DTM validation was for the VV data of the region in England. However, the lowest IoU (0.63) was obtained for VH images from Cambodia compared with the DTM water masks. Regarding the IoU per class, the highest IoU of the water class was for the Chan-Vese method in the England model performed with VV data (0.69) and the lowest for the Poland area with VV images (0.49). The non-water class provided the highest IoU for VH Italy data (0.93) and the lowest for Cambodia VH data (0.71).

For the Gaussian Mixture model, the highest IoU (0.74) provided for DTM validation was for the region in England. However, the lowest IoU (0.64) was obtained for Cambodia. In the case of IoU per class, the highest IoU of the water class was for the Brazil study area (0.67) and the lowest for the Italy area (0.48). The non-water class provided the highest IoU for Italy data (0.91) and the lowest for Cambodia data (0.71).

For the spectral clustering method, the highest IoU (0.72) provided for DTM validation was for the region in England. The lowest IoU (0.27) was obtained for the Italy study area. Regarding the IoU per class, the highest IoU of the water class was for the Brazil study area (0.66) and the lowest for the Italy area (0.12). The non-water class provided the highest IoU for England data (0.80) and the lowest for Italy data (0.42).

From benchmarking methods, the highest IoU values for DTM validation were obtained from the Chan-Vese method applied to VV data (Cambodia, England, and Italy study areas) and the Gaussian mixture model (Brazil and Poland study areas). When comparing the FPGNN outputs, which obtained the highest average IoU from tested thresholds, with the best unsupervised method's results, the FPGNN method had similar or slightly higher IoU for all study cases. In England, the water class was classified better with Chan Vese segmentation with VV data, whereas the non-water

class obtained higher accuracy with FPGNN. However, the comparison with the DTM is not reliable in the England area due to the fact that when the elevation of the water in the river is low, the river patch is not visible in the SAR images, whereas it is shown as water in the DTM mask. Due to the numerous misclassified pixels on the benchmarking method's results covered with water pixels on the DTM water mask, the water mask from benchmarking methods had a higher water class IoU than the FPGNN water mask, where no water pixels were detected.

4.2 Impact of water elevation on effectiveness of FPGNN

For the study cases in Brazil and Cambodia (Fig. 4a, b), there are some visible dependences between the IoU and the water level. The IoU of the water class increased when the water level in the river increased, and conversely for the non-water class, in the MNDWI validation. This dependence is more visible for the DTM validation results due to the greater variation of the IoU. The IoU of the water class increased during floods in almost the whole analyzed area, so each misclassification has a smaller impact on the IoU value than when the water level is low during the dry season. A similar relationship can be noticed for the Cambodia site. In this case, our method provided a higher IoU for water class than the Chan-Vese VV and GMM algorithms during low water elevation, i.e. when the difference in the water class IoU was the greatest.

For the study area in the UK, the lowest IoU values were obtained when low water elevation was in the river independently of the method used (Fig. 4c). The imaged river is 20 m wide, which is only double the pixel size of the SAR images. Therefore, the river area when the water level is low is less visible on the SAR data, while it is detected on the MNDWI. The benchmarking methods performed better in that case and classified the river as water class; however, at the same time, it misclassified many agricultural fields. This resulted in a low IoU for both classes during low water elevation. For the same cases, our algorithm could not detect the river area but classified the non-water areas better in both validation methods. On 20 February 2016, the water class IoU for the FPGNN was considerably lower than for the Chan-Vese and GMM methods. The registered backscattering for the water is higher than on other days due to waves on the water's surface. The FPGNN mostly analyzed the texture of the image during training. The higher intensity of the water pixels on the image from 20 February 2016 compared to the images from the other days caused the water to not be detected by our method.

The results for the Italy area are characterized with steady IoU values above 0.9 for the non-water class (Fig. 4d). The IoU of the water class is significantly lower than that of the non-water class because water occupies only a small part of the area. Most of the water areas are located inside the river valley and appear outside it only during floods. There is one exception, in which the IoU for both classes decreased significantly (3 October 2020). This low result was caused by the significant difference between the radar and MNDWI images, which were obtained during a flood event. The optical image was acquired about 7 hours earlier than the SAR image. The registered flood was a dynamic phenomenon, which resulted in a considerable change in the water extent between the acquisitions. Other days with a lower water class IoU (below 0.5) are 11 and 13 April 2020, where farmlands without vegetation were misclassified in the SAR data as water due to their smooth surface. However, our method obtained a higher IoU for both classes than the Otsu because it misclassified fewer agricultural fields. This is the effect of extracting contextual information by the convolutional layers in our model.

The IoU for the area in Poland increased with the decreasing water elevation for our method (Fig. 4e). The benchmarking algorithms obtained similar results for the water class as our method, however, their IoU decreased significantly when the water elevation in the river started decreasing. This was caused by numerous misclassified pixels of the non-water class by Otsu. The FPGNN performed better independent of the water elevation, especially during the low water stage, and obtained a significantly higher IoU for both classes. The lowest IoU for the water class (below 0.4) was for images from the days between 19 March and 9 April 2018 in the MNDWI validation (for FPGNN and the benchmarking methods). This was caused by the optical images being registered when the river and the floodplains were partially or completely frozen. The ice on the river has higher backscattering on radar images than open water [56]. Effectively water pixels were only labeled on the SAR data in places where the ice had melted.

4.3 Visual interpretation of results

Based on visual comparisons of the water masks obtained with data from various sensors, we noticed the main drawbacks of radar and optical satellite data (Fig. 5). The main visible difference in the water masks from SAR and MNDWI from the optical sensor was the shift in the water area. It was caused by the fact that the SAR sensor sent its signal sideways, and the terrain was illuminated only from one side. Tall objects along the river, such as trees and buildings, also influenced the shift of the mapped water area in the SAR image. Also, despite the speckle filtering in SAR, some noise in the pixels remained. The noise decreased the classification efficiency, especially for pixel-based

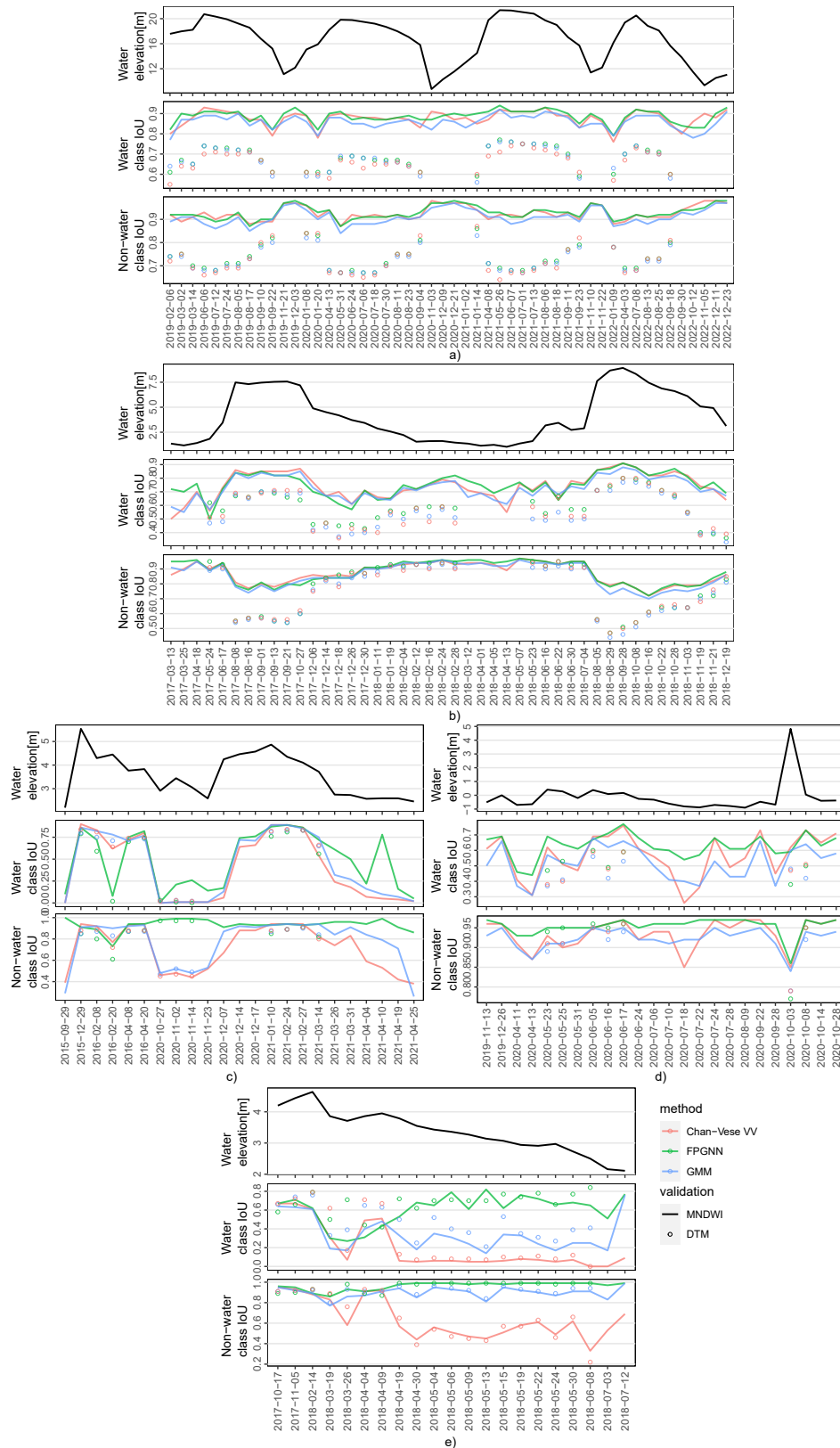


Figure 4: Comparisons of IoU for days of optical image acquisition for sites located in Brazil (a), Cambodia (b), Italy (c), England (d) and Poland (e). Panel for each site includes three plots: observed water elevation, calculated water and non-water class IoU for the FPGNN, GMM and SC methods in MNDWI and DTM validation.

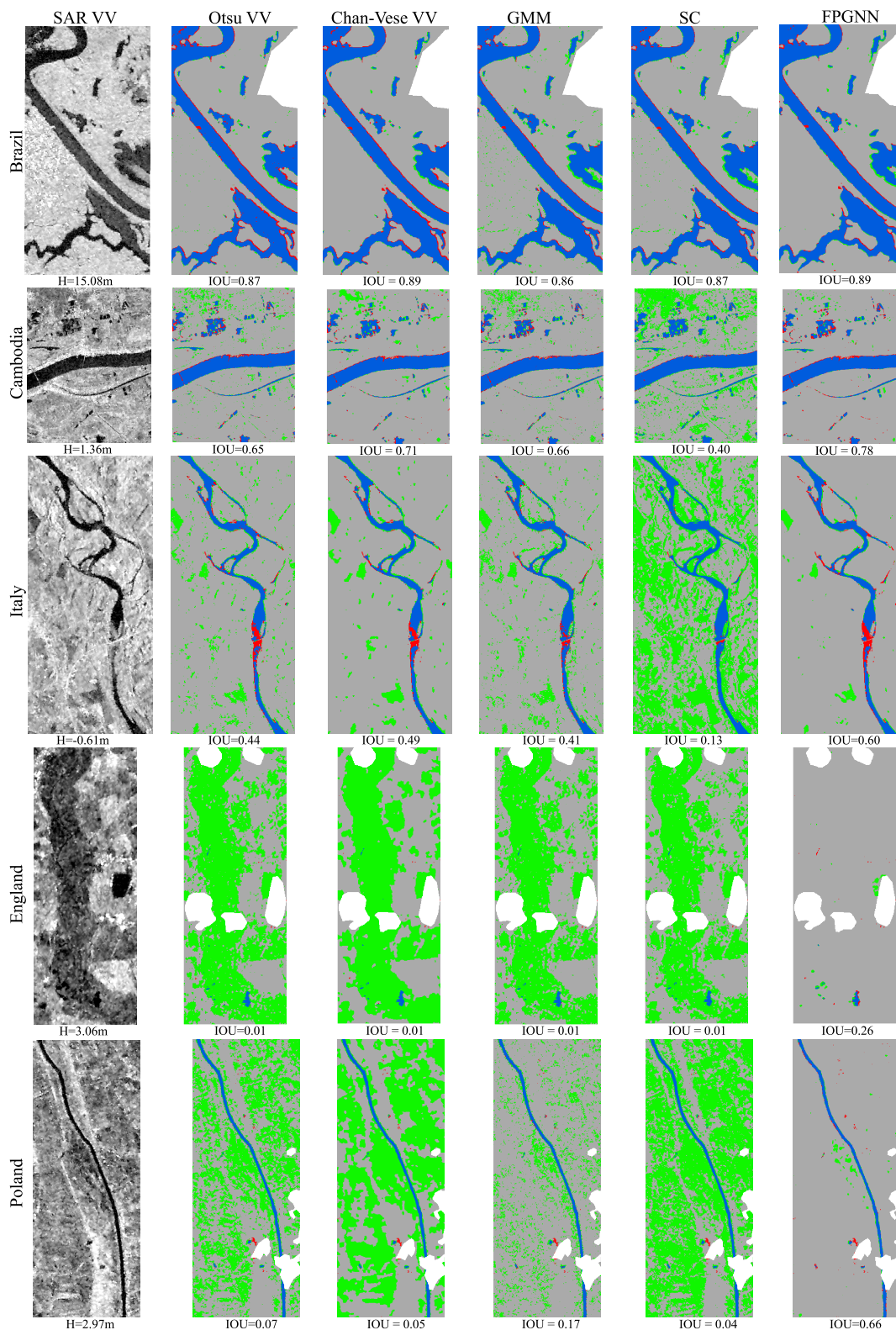


Figure 5: Contingency maps obtained from a pixel-to-pixel comparison between the MNDWI water masks and FPGNN or the benchmarking methods for all study sites for low water elevation. True positives are shown in blue, true negatives in gray, false positives in green, and false negatives in red.

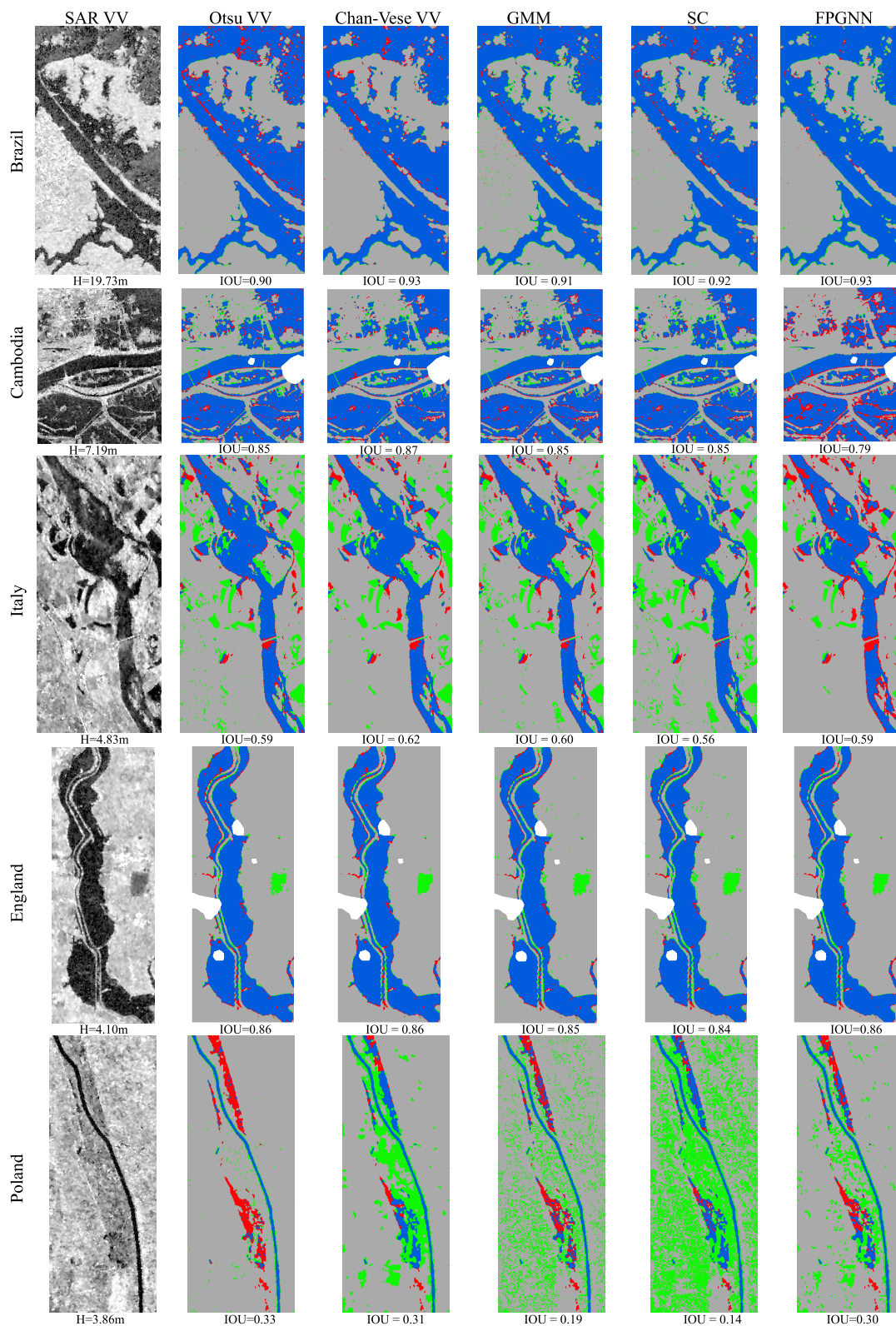


Figure 6: Contingency maps obtained from a pixel-to-pixel comparison between the MNDWI water masks and FPGNN or the benchmarking methods for all study sites for high water elevation. True positives are shown in blue, true negatives in gray, false positives in green, and false negatives in red.

classification method. In contrast, the water mask obtained with optical data was more homogeneous. Another observed effect on the SAR water masks was their worse preservation of the narrow terrain objects than on the MNDWI images due to the speckle filtering process. The water areas on the radar images were identified by the low intensity of backscattering from their smooth surface. The roughness of the water surface could change due to strong wind or possible water cascades, which resulted in increasing the backscattering and misclassification of pixels (the Italy area). In contrast, such phenomena did not influence the water extent based on the optical images. Moreover, the SAR sensor was more sensitive at detecting objects on the water surface, such as bridges, due to their high roughness compared to water. On the MNDWI results, these objects were not classified as non-water because of the low spatial resolution of the short-infrared band.

The differences between the results for Otsu and FPGNN were not only in their IoU values but also in visual comparison. One of main advantages of Otsu was that it better prevented narrow line objects, such as tributary rivers, roads and bridges. The FPGNN omitted those objects due to the applied 3x3 filters in the convolutional layers and the 2x2 windows in the polling layers. Other studies showed that supervised deep learning methods could quite accurately detect line objects [21]. However, our method did not use any ground-truth water masks, hence, it lost this information. On the other hand, this allowed the FPGNN to classify correctly the single, bright pixels in the water segments, which were misclassified by the Otsu thresholding. A similar effect of more homogenous water segments achieved the Chan-Vese segmentation. However, this method slightly enlarged the water segments, which negatively influenced the water map accuracy. The FPGNN performed significantly better than benchmarking methods in distinguishing between water bodies and agricultural areas without vegetation because the neural network extracted contextual features from the images.

For the sites in Brazil and Cambodia, the water masks for FPGNN and benchmarking methods were similar for SAR images registered during low and high water elevation. In the case of the England, Poland, and Italy study areas, the accuracy achieved for flood images was comparable. However, when the water regions occupied a small part of the areas analyzed, the performance of all of the tested benchmarking methods considerably decreased, and there were visible lots of misclassified pixels. The Otsu method has been known to provide unstable results when there is a small area of water bodies and large non-water features in the image [57]. Whereas, the FPGNN correctly classified the water segments on those specific images. Our method produced more accurate results, especially for SAR images with no visible river (the England area).

4.4 Advantages and limitations

The main advantage of our method is that it does not require labeled data showing water areas prepared by experts. The approach needs only the preprocessed times series of radar data and the water elevations for the corresponding days. The SAR data preprocessing steps can be automated by remote sensing software or performed using online APIs (ASF, Sentinel Hub). Hydrological observations do not need to be processed; however, requiring these data limits the method's application to river areas in which water gauge stations are present. However, our study shows that the method works not only in the proximity of the river gauge, but at least 7 km upstream or downstream. We expect this distance should be greater, i.e. our method should be valid for a regional-size catchment scale, which should be verified in a follow-up study.

The most important limitation is that the method does not work for river areas where the imaged riverbed does not change its width while the elevation of the water changes significantly. In that case, there is no relation between the flooded area and the elevation of the water, and the model cannot learn from those data. Another limitation is the necessity to train the new model for each area. We expect that the transfer learning approach should be beneficial in our method, however, this should be verified in a follow-up study. In addition, the input data should contain the SAR images and water elevation presenting the river during different stages (flood, drought). Based on the England area, we noticed another limitation – the width of the river. Our approach performed better for rivers at least twice as wide as the spatial resolution of the input radar data, including when the river stage is low. However, this drawback can be solved by applying images with higher spatial resolution. The results of this study suggest that the frequent presence of ice on the surface of the water could significantly influence the action of our method due to the lower correlation between water extent area and water elevation. A similar problem could occur in areas with vegetation obscuring the water. In addition, data such as optical satellite images or DTM are required if one wishes to fully verify the results against ground-truth.

5 Summary

In this paper, we proposed a physics-guided neural network for flood area detection (FPGNN) using SAR data and river gauge observations. The assumption in our approach was a monotonically non-decreasing relation between a

local river water elevation and the flooded area. We applied time-series SAR images and water elevation observations as input datasets in our method. The FPGNN was tested for five study sites characterized by various climates and land cover types.

Our results show that the relationship between SAR-derived flood extents and water elevations occurs and can be used to train a neural network by applying the correlation coefficient between the mentioned variables as a loss function. The FPGNN provides classification models that produce more accurate water masks for different areas than the compared methods. The highest differences between results are for water maps showing rivers during low water elevations, when small part of SAR image is covered by the water. While, the other unsupervised approaches mismatch the water class in many pixels. However, the application of FPGNN is limited by river valley characteristics, such as the shape of the riverbed, the density and height of vegetation, and the occurrence of ice cover, which can decrease the correlation between the water extent and the water elevation.

References

- [1] G. Xin and Z. Yindi, "Flood inundation Monitoring in Ningxiang of Hunan Province Based on Sentinel-1A SAR," *Remote sensing technology and application*, vol. 33, no. 4, pp. 646–656, 2018.
- [2] M. Rättich, S. Martinis, and M. Wieland, "Automatic Flood Duration Estimation Based on Multi-Sensor Satellite Data," *Remote Sensing*, vol. 12, no. 4, p. 643, Feb. 2020.
- [3] Y. Yamada, "Detection of flood-inundated area and relation between the area and micro-geomorphology using SAR and GIS," in *IGARSS 2001. Scanning the Present and Resolving the Future. Proceedings. IEEE 2001 International Geoscience and Remote Sensing Symposium (Cat. No.01CH37217)*, ser. IGARSS-01. IEEE, 2001.
- [4] S. Long, T. E. Fatoyinbo, and F. Policelli, "Flood extent mapping for Namibia using change detection and thresholding with SAR," *Environmental Research Letters*, vol. 9, no. 3, p. 035002, Mar. 2014.
- [5] P. Manjusree, L. Prasanna Kumar, C. M. Bhatt, G. S. Rao, and V. Bhanumurthy, "Optimization of threshold ranges for rapid flood inundation mapping by evaluating backscatter profiles of high incidence angle SAR images," *International Journal of Disaster Risk Science*, vol. 3, no. 2, pp. 113–122, Jun. 2012.
- [6] Q. Tan, S. Bi, J. Hu, and Z. Liu, "Measuring lake water level using multi-source remote sensing images combined with hydrological statistical data," in *IEEE International Geoscience and Remote Sensing Symposium, 2004. Proceedings. 2004.* IEEE, 2004.
- [7] M. S. Horritt, D. C. Mason, and A. J. Luckman, "Flood boundary delineation from Synthetic Aperture Radar imagery using a statistical active contour model," *International Journal of Remote Sensing*, vol. 22, no. 13, pp. 2489–2507, Jan. 2001.
- [8] S. Martinis, A. Twele, and S. Voigt, "Towards operational near real-time flood detection using a split-based automatic thresholding procedure on high resolution TerraSAR-X data," *Natural Hazards and Earth System Sciences*, vol. 9, no. 2, pp. 303–314, Mar. 2009.
- [9] Y. Bazi, L. Bruzzone, and F. Melgani, "An unsupervised approach based on the generalized Gaussian model to automatic change detection in multitemporal SAR images," *IEEE Transactions on Geoscience and Remote Sensing*, vol. 43, no. 4, pp. 874–887, Apr. 2005.
- [10] R. Manavalan, "SAR image analysis techniques for flood area mapping - literature survey," *Earth Science Informatics*, vol. 10, no. 1, pp. 1–14, Oct. 2016.
- [11] M. Chini, R. Hostache, L. Giustarini, and P. Matgen, "A Hierarchical Split-Based Approach for Parametric Thresholding of SAR Images: Flood Inundation as a Test Case," *IEEE Transactions on Geoscience and Remote Sensing*, vol. 55, no. 12, pp. 6975–6988, Dec. 2017.
- [12] X. Shen, E. N. Anagnostou, G. H. Allen, G. Robert Brakenridge, and A. J. Kettner, "Near-real-time non-obstructed flood inundation mapping using synthetic aperture radar," *Remote Sensing of Environment*, vol. 221, pp. 302–315, Feb. 2019.
- [13] F. Frappart, F. Seyler, J.-M. Martinez, J. G. León, and A. Cazenave, "Floodplain water storage in the Negro River basin estimated from microwave remote sensing of inundation area and water levels," *Remote Sensing of Environment*, vol. 99, no. 4, pp. 387–399, Dec. 2005.
- [14] W. Ahmad and D. Kim, "Estimation of flow in various sizes of streams using the Sentinel-1 Synthetic Aperture Radar (SAR) data in Han River Basin, Korea," *International Journal of Applied Earth Observation and Geoinformation*, vol. 83, p. 101930, Nov. 2019.

- [15] S. Schlaffer, M. Chini, R. Poppl, R. Hostache, and P. Matgen, “Monitoring of Inundation Dynamics in the North-American Prairie Pothole Region using Sentinel-1 Time Series,” in *IGARSS 2018 - 2018 IEEE International Geoscience and Remote Sensing Symposium*. IEEE, Jul. 2018.
- [16] L. Pulvirenti, G. Boni, N. Pierdicca, M. Fiorini, and R. Rudari, “Combined use of multi-temporal COSMO-SkyMed data and a hydrodynamic model to monitor flood dynamics,” in *2014 IEEE Geoscience and Remote Sensing Symposium*. IEEE, Jul. 2014.
- [17] S. Schlaffer, P. Matgen, M. Hollaus, and W. Wagner, “Flood detection from multi-temporal SAR data using harmonic analysis and change detection,” *International Journal of Applied Earth Observation and Geoinformation*, vol. 38, pp. 15–24, Jun. 2015.
- [18] F. Cian, M. Marconcini, and P. Ceccato, “Normalized Difference Flood Index for rapid flood mapping: Taking advantage of EO big data,” *Remote Sensing of Environment*, vol. 209, pp. 712–730, May 2018.
- [19] J. E. Ball, D. T. Anderson, and C. S. Chan, “Comprehensive survey of deep learning in remote sensing: theories, tools, and challenges for the community,” *Journal of Applied Remote Sensing*, vol. 11, no. 04, p. 1, Sep. 2017.
- [20] L. Ma, Y. Liu, X. Zhang, Y. Ye, G. Yin, and B. A. Johnson, “Deep learning in remote sensing applications: A meta-analysis and review,” *ISPRS Journal of Photogrammetry and Remote Sensing*, vol. 152, pp. 166–177, Jun. 2019.
- [21] R. Sadiq, Z. Akhtar, M. Imran, and F. Offi, “Integrating remote sensing and social sensing for flood mapping,” *Remote Sensing Applications: Society and Environment*, vol. 25, p. 100697, Jan. 2022.
- [22] J. Wang, S. Wang, F. Wang, Y. Zhou, Z. Wang, J. Ji, Y. Xiong, and Q. Zhao, “FWENet: a deep convolutional neural network for flood water body extraction based on SAR images,” *International Journal of Digital Earth*, vol. 15, no. 1, pp. 345–361, Feb. 2022.
- [23] G. I. Drakonakis, G. Tsagkatakis, K. Fotiadou, and P. Tsakalides, “OmbriaNet-Supervised Flood Mapping via Convolutional Neural Networks Using Multitemporal Sentinel-1 and Sentinel-2 Data Fusion,” *IEEE Journal of Selected Topics in Applied Earth Observations and Remote Sensing*, vol. 15, pp. 2341–2356, 2022.
- [24] A. S. Arnesen, T. S. Silva, L. L. Hess, E. M. Novo, C. M. Rudorff, B. D. Chapman, and K. C. McDonald, “Monitoring flood extent in the lower Amazon River floodplain using ALOS/PALSAR ScanSAR images,” *Remote Sensing of Environment*, vol. 130, pp. 51–61, Mar. 2013.
- [25] L. C. Smith, B. L. Isacks, A. L. Bloom, and A. B. Murray, “Estimation of Discharge From Three Braided Rivers Using Synthetic Aperture Radar Satellite Imagery: Potential Application to Ungaged Basins,” *Water Resources Research*, vol. 32, no. 7, pp. 2021–2034, Jul. 1996.
- [26] D. Kim, H. Lee, A. Laraque, R. M. Tshimanga, T. Yuan, H. C. Jung, E. Beighley, and C.-H. Chang, “Mapping spatio-temporal water level variations over the central Congo River using PALSAR ScanSAR and Envisat altimetry data,” *International Journal of Remote Sensing*, vol. 38, no. 23, pp. 7021–7040, Aug. 2017.
- [27] T. Berezowski, T. Bielinski, and J. Osowicki, “Flooding Extent Mapping for Synthetic Aperture Radar Time Series Using River Gauge Observations,” *IEEE Journal of Selected Topics in Applied Earth Observations and Remote Sensing*, vol. 13, pp. 2626–2638, 2020.
- [28] T. Berezowski, S. Niemiec, and A. Chybicki, “Floodsar: Automatic mapping of river flooding extent from multitemporal SAR imagery,” *SoftwareX*, vol. 26, p. 101717, May 2024.
- [29] R. Yadav, A. Nascetti, H. Azizpour, and Y. Ban, “Unsupervised flood detection on SAR time series using variational autoencoder,” *International Journal of Applied Earth Observation and Geoinformation*, vol. 126, p. 103635, Feb. 2024.
- [30] X. Jiang, S. Liang, X. He, A. D. Ziegler, P. Lin, M. Pan, D. Wang, J. Zou, D. Hao, G. Mao, Y. Zeng, J. Yin, L. Feng, C. Miao, E. F. Wood, and Z. Zeng, “Rapid and large-scale mapping of flood inundation via integrating spaceborne synthetic aperture radar imagery with unsupervised deep learning,” *ISPRS Journal of Photogrammetry and Remote Sensing*, vol. 178, pp. 36–50, Aug. 2021.
- [31] E. Nemni, J. Bullock, S. Belabbes, and L. Bromley, “Fully Convolutional Neural Network for Rapid Flood Segmentation in Synthetic Aperture Radar Imagery,” *Remote Sensing*, vol. 12, no. 16, p. 2532, Aug. 2020.
- [32] H. Parikh, S. Patel, and V. Patel, “Classification of SAR and PolSAR images using deep learning: a review,” *International Journal of Image and Data Fusion*, vol. 11, no. 1, pp. 1–32, Aug. 2019.
- [33] S. Klemenjak, B. Waske, S. Valero, and J. Chanussot, “Automatic Detection of Rivers in High-Resolution SAR Data,” *IEEE Journal of Selected Topics in Applied Earth Observations and Remote Sensing*, vol. 5, no. 5, pp. 1364–1372, Oct. 2012.

- [34] B. Han and A. Basu, “Level Sets Guided by SoDEF-Fitting Energy for River Channel Detection in SAR Images,” *Remote Sensing*, vol. 15, no. 13, p. 3251, Jun. 2023.
- [35] N. Gasnier, L. Denis, R. Fjortoft, F. Liege, and F. Tupin, “Narrow River Extraction From SAR Images Using Exogenous Information,” *IEEE Journal of Selected Topics in Applied Earth Observations and Remote Sensing*, vol. 14, pp. 5720–5734, 2021.
- [36] A. Daw, A. Karpatne, W. D. Watkins, J. S. Read, and V. Kumar, *Physics-Guided Neural Networks (PGNN): An Application in Lake Temperature Modeling*. Chapman and Hall/CRC, Jun. 2022, pp. 353–372.
- [37] J. Chen, P. Tang, T. Rakstad, M. Patrick, and X. Zhou, “Augmenting a deep-learning algorithm with canal inspection knowledge for reliable water leak detection from multispectral satellite images,” *Advanced Engineering Informatics*, vol. 46, p. 101161, Oct. 2020.
- [38] Z. Huang, X. Yao, Y. Liu, C. O. Dumitru, M. Datcu, and J. Han, “Physically explainable CNN for SAR image classification,” *ISPRS Journal of Photogrammetry and Remote Sensing*, vol. 190, pp. 25–37, Aug. 2022.
- [39] J. S. Read, X. Jia, J. Willard, A. P. Appling, J. A. Zwart, S. K. Oliver, A. Karpatne, G. J. A. Hansen, P. C. Hanson, W. Watkins, M. Steinbach, and V. Kumar, “Process-Guided Deep Learning Predictions of Lake Water Temperature,” *Water Resources Research*, vol. 55, no. 11, pp. 9173–9190, Nov. 2019.
- [40] K. Hogenson, S. A. Arko, B. Buechler, R. Hogenson, J. Herrmann, and A. Geiger, “Hybrid Pluggable Processing Pipeline (HyP3): A cloud-based infrastructure for generic processing of SAR data,” in *AGU Fall Meeting Abstracts*, vol. 2016, Dec. 2016, pp. IN21B–1740.
- [41] SNIRH, (2023) Sistema Nacional de Informações sobre Recursos Hídricos/ (National Water Resources Information System NWRIS). (In Portuguese). Accessed: Jan. 20, 2023. [Online]. Available: <https://www.snirh.gov.br/>.
- [42] IAPR, (2023) Agenzia Interregionale per il fiume Po (AIPo) / (Interregional Agency for the Po River). (In Italian). Accessed: Jan. 20, 2023. [Online]. Available: <https://www.agenziapo.it/content/monitoraggio-idrografico-0>.
- [43] MRC, (2023) Mekong River Commission (MRC) Data Portal. Accessed: Jan. 20, 2023. [Online]. Available: <https://portal.mrcmekong.org/time-series/water-level>.
- [44] PIMWM, (2023) Dane publiczne IMGW-PIB/ (Public data PIMWM)). (In Polish). Accessed: Jan. 20, 2023. [Online]. Available: <https://dane.imgw.pl/>.
- [45] EA, (2023) The Environment Agency: Hydrology Data API. Accessed: Jan. 20, 2023. [Online]. Available: <https://environment.data.gov.uk/hydrology>.
- [46] —, (2023) The Environment Agency: Defra Survey Data Download. Accessed: Mar. 30, 2023. [Online]. Available: <https://environment.data.gov.uk/survey>.
- [47] HOGC, (2023) Digital Terrain Model - Head Office of Geodesy and Cartography. Accessed: Mar. 30, 2023. [Online]. Available: <https://dane.gov.pl/en/dataset/2027,numeryczny-model-terenu-nmt>.
- [48] H. Xu, “Modification of normalised difference water index (NDWI) to enhance open water features in remotely sensed imagery,” *International Journal of Remote Sensing*, vol. 27, no. 14, pp. 3025–3033, Jul. 2006.
- [49] E. Shelhamer, J. Long, and T. Darrell, “Fully Convolutional Networks for Semantic Segmentation,” *IEEE Transactions on Pattern Analysis and Machine Intelligence*, vol. 39, no. 4, pp. 640–651, Apr. 2017.
- [50] Y. Du, Y. Zhang, F. Ling, Q. Wang, W. Li, and X. Li, “Water Bodies Mapping from Sentinel-2 Imagery with Modified Normalized Difference Water Index at 10-m Spatial Resolution Produced by Sharpening the SWIR Band,” *Remote Sensing*, vol. 8, no. 4, p. 354, Apr. 2016.
- [51] N. Otsu, “A Threshold Selection Method from Gray-Level Histograms,” *IEEE Transactions on Systems, Man, and Cybernetics*, vol. 9, no. 1, pp. 62–66, Jan. 1979.
- [52] T. Chan and L. Vese, “An Active Contour Model without Edges,” in *Scale-Space Theories in Computer Vision*, M. Nielsen, P. Johansen, O. F. Olsen, and J. Weickert, Eds. Berlin, Heidelberg: Springer Berlin Heidelberg, 1999, pp. 141–151.
- [53] C. M. Bishop, *Pattern Recognition and Machine Learning (Information Science and Statistics)*. Berlin, Heidelberg: Springer-Verlag, 2006.
- [54] U. von Luxburg, “A tutorial on spectral clustering,” *Statistics and Computing*, vol. 17, no. 4, pp. 395–416, Aug. 2007.
- [55] M. Gierszewska and T. Berezowski, “On the Role of Polarimetric Decomposition and Speckle Filtering Methods for C-Band SAR Wetland Classification Purposes,” *IEEE Journal of Selected Topics in Applied Earth Observations and Remote Sensing*, vol. 15, pp. 2845–2860, 2022.

- [56] D. Yan, C. Huang, N. Ma, and Y. Zhang, "Improved Landsat-Based Water and Snow Indices for Extracting Lake and Snow Cover/Glacier in the Tibetan Plateau," *Water*, vol. 12, no. 5, p. 1339, May 2020.
- [57] X. Yang, S. Zhao, X. Qin, N. Zhao, and L. Liang, "Mapping of Urban Surface Water Bodies from Sentinel-2 MSI Imagery at 10 m Resolution via NDWI-Based Image Sharpening," *Remote Sensing*, vol. 9, no. 6, p. 596, Jun. 2017.